THE ASTROPHYSICAL JOURNAL, 997:137 (7pp), 2026 February 1 https://doi.org/10.3847/1538-4357/ae25e6

First in Situ Estimates of the Sheath Resistance for the PSP/FIELD Antenna: Employing an Electron Shot Noise Model

Xianming Zheng[1,2,3], Mihailo M. Martinović[3,4], Kristopher G. Klein[4], Viviane Pierrard[5,6], Mingzhe Liu[3,7], Yang Wang[1], Tao Wu[1], Winry Ember[7], Jingchun Li[8], Naomi Maruyama[9], Yutian Chi[1], Yao Yao[1], Bingkun Yu[1,2], and Xianghui Xue[2]
[1] Institute of Deep Space Sciences, Deep Space Exploration Laboratory, Hefei 230026, People's Republic of China
[2] CAS Key Laboratory of Geospace Environment, Department of Geophysics and Planetary Sciences, University of Science and Technology of China, Hefei, People's Republic of China; bkyu@ustc.edu.cn, xuexh@ustc.edu.cn
[3] LESIA, Observatoire de Paris, Meudon, France
[4] Lunar and Planetary Laboratory, University of Arizona, Tucson, AZ, USA
[5] Royal Belgian Institute for Space Aeronomy (BIRA-IASB), Space Physics, Solar-Terrestrial Center of Excellence, Brussels, Belgium
[6] Earth and Life Institute—Climate Science (ELI-C), Université Catholique de Louvain, Louvain-la-Neuve, Belgium
[7] Space Sciences Laboratory, University of California, Berkeley, CA 94720-7450, USA
[8] Shenzhen Key Laboratory of Nuclear and Radiation Safety, Institute for Advanced Study in Nuclear Energy & Safety, College of Physics and Optoelectronic Engineering, Shenzhen University, Shenzhen 518060, People's Republic of China
[9] Space Weather Prediction Center, National Oceanic and Atmospheric Administration, Boulder, CO, USA
Received 2025 September 17; revised 2025 November 26; accepted 2025 November 26; published 2026 January 20

Abstract

Quasi-thermal noise is an important diagnostic tool for measuring electron density and temperature in space plasmas, with its low-frequency range being dominated by electron shot noise. However, previous missions have shown that conventional shot noise models often yield poor fits in the low frequency ($f < f_p$), limiting the accurate characterization of electron parameters. To address this issue, we introduce an effective sheath resistance into the previous model, thereby establishing a calibrated shot noise model that improves measurements of electron parameters in the inner heliosphere. Methodologically, we applied the steep-descent and Levenberg–Marquardt method algorithm to determine the electron density and temperature above the plasma frequency; we then isolate the pure shot noise by subtracting other noise sources; and finally, we derive the antenna impedance using measurements below the plasma frequency (f_p). Based on Parker Solar Probe (PSP) observations during PSP Encounter 4 $\sim$ 8 (with unbiased antennas operating in the dipole regime), we obtain an effective antenna capacitance of 8.30 $\pm$ 0.21pF and an effective resistance in the range of 0.5 $\sim$ 4 MΩ, with their radial of the capacitances and resistances of $r^{-0.072 \pm 0.001}$ and $r^{2.57 \pm 0.02}$, respectively.

Unified Astronomy Thesaurus concepts: Space plasmas (1544); Discrete radio sources (389); Solar wind (1534); Radio spectroscopy (1359)

1. Introduction

Understanding the physics of the solar wind and other weakly collisional plasma environments depends on high-quality in situ measurement of electron and ion distributions. Comprehensive data sets of such measurements are provided by several electrostatic analyzers on board various missions (R. P. Lin et al. 1995; D. Young et al. 2005; J. A. Sauvaud et al. 2008; P. L. Whittlesey et al. 2020), but these measurements suffer from multiple limiting factors, such as varying spacecraft electrostatic potential (M. Pulupa et al. 2014), secondary electron emission (P. J. Kellogg 1981), magnetic field effects (M. Moncuquet et al. 1995; P. Dazzi et al. 2025; X. Zheng et al. 2025), and the temporal variations in the instrument's internal calibration activities, known as bias sweeps (M. F. Diaz-Aguado et al. 2021a).

Quasi-thermal noise (QTN) has been routinely used on various missions in the solar wind: Ulysses (K. Issautier et al. 1996; K. Issautier et al. 1999; G. Le Chat et al. 2011), Wind (K. Issautier et al. 2005; M. M. Martinović et al. 2020), STEREO (I. Zouganelis et al. 2010; M. Martinović et al. 2016), and planetary missions like CASSINI (M. Moncuquet et al. 2005). However, in previous applications detections, the shot noise model has always been considered to be purely capacitive (I. Zouganelis et al. 2010; M. Martinović et al. 2016). This model is no longer accurate when the instrument covers a wide range of frequencies below the plasma frequency, $f_p = \frac{1}{2\pi}\sqrt{\frac{ne^2}{\varepsilon_0 m_e}}$, where n denotes the electron number density, e is the elementary charge, ε_0 is the vacuum permittivity, and m_e is the electron mass.

The Parker Solar Probe (PSP) spacecraft (N. Fox et al. 2016) was launched on 2018 August 12. Its orbital perihelia have decreased from 35.7 to 9.86 R_S (solar radii) from the solar surface over the first 5 yr of the mission. On board PSP are four instruments—Fields (FIELDS; S. D. Bale et al. 2016) experiment, Solar Wind Electrons Alphas and Protons investigation (J. C. Kasper et al. 2016; A. W. Case et al. 2020; P. L. Whittlesey et al. 2020; R. Livi et al. 2022), Integrated Science Investigation of the Sun (D. McComas et al. 2016), and Wide-field Imager for Solar Probe (A. Vourlidas et al. 2016)—that are collaborating to provide both in situ and remote observations. Previously, M. Moncuquet et al. (2020), M. Maksimovic et al. (2020), M. M. Martinović et al. (2022), and M. Liu et al. (2021, 2023) derived preliminary solar wind plasma parameters using QTN spectroscopy on board PSP, and most of them considered that the shot noise for PSP at perihelion is negligible above plasma frequency ($f > f_p$) (N. Meyer-Vernet et al. 2017).

The potential difference between the spacecraft–antenna system and the surrounding plasma causes the antenna to attract or repel charged particles, forming a plasma sheath. Its thickness, comparable to the electron Debye length, significantly affects the antenna's electrical response. In an equivalent circuit, this effect appears as an additional sheath resistance, dominating the antenna–plasma coupling at low frequencies and diminishing at high frequencies. Accounting for the sheath as an extra impedance allows the shot noise model to better match PSP/FIELDS observations (M. M. Martinović et al. 2022; X. Zheng et al. 2024b).

The primary objective of this paper is to calculate the effective sheath resistance (the equivalent resistance between the plasma and the antenna terminals) and the capacitance from the shot noise spectrum. To accomplish this objective, in Section 2, we derive the total QTN model and obtain the calibration shot noise model by adding the effective sheath resistances and describe how to calculate the real shot noise from the observations. Then, in Section 3, we calculate the sheath resistances and capacitance for each QTN spectroscopy for the period when antenna was unbiased. Additionally, we compute the radial profiles for both parameters, statistically analyzing their distribution. The results show great agreement with the previous results for antenna capacitance (D. P. Cauffman & D. A. Gurnett 1972; D. Gurnett 1998). Finally, in Section 4, we conclude by discussing the future applications of this model, particularly in biased conditions for PSP antennas. We also address potential limitations that may arise when using this model.

2. Methodology

2.1. Electron Shot Noise on Parker Solar Probe

The QTN method can be applied to the measurement at frequency above ion plasma angular frequency $\omega \gg \omega_i$ up to the range of significant galactic radiation. The observed signal comprises three primary components: the electron QTN $V_{\rm qtn}^2$, generated by the thermal motion of ambient electrons; the proton noise V_P^2, arising from the thermal motion of protons and Doppler-shifted by the bulk velocity of the solar wind (here, we neglect the electron Doppler shift, since the thermal velocity $V_{\rm th}$ is much greater than the drift velocity V_D, N. Meyer-Vernet et al. 2017; N. Meyer-Vernet & A. Lecacheux 2024); and the electron shot noise $V_{\rm sn}^2$. For $f < f_p$, the previous shot noise model for a wire dipole is defined by the following expression (N. Meyer-Vernet 1983; M. Martinović et al. 2016; M. M. Martinović et al. 2022):

$$V_{\rm sn}^2 = 2e^2 N_{\rm impact}\, |Z|^2. \tag{1}$$

Here, Z is the antenna impedance and $N_{\rm impact}$ is the number of impacts on the antenna surface per unit (J. Laframboise & L. Parker 1973; M. Martinović 2016; M. Martinović et al. 2016). At frequencies below f_p, the antenna impedance Z is capacitive, with an absolute value defined by (N. Meyer-Vernet & C. Perche 1989; S. D. Bale et al. 2008)

$$|Z|^2 = \frac{1}{\omega^2 C_a^2} = \frac{1}{f^2\,(2\pi C_a)^2}, \tag{2}$$

where C_a is antenna capacitance (M. Martinović et al. 2016; W. Ember et al. 2024a).

The PSP/FIELDS instruments use four 2 m monopole antennas, with each antenna having an average radius of 1.5 mm. The signals from the antenna are processed by the Low Frequency Receiver (LFR), which has an operational frequency range from 10 kHz to 1.7 MHz and a spectral resolution of $\Delta f/f \approx 4.5\%$ (M. Pulupa et al. 2017). At frequencies just below f_p, the signal scales with $V_{\rm qtn}^2 \propto \sqrt{T_c}$. For $f \ll f_p$, $V^2 \propto f^{-2}$ (M. M. Martinović et al. 2020), with the capacitive contribution becoming dominant. Finally, at the lowest measured frequencies, the shot noise intensity flattens, indicating transition to resistively coupled regime. For PSP, the antenna can be modeled using four electronic components: the sheath impedance Z_s (an effective sheath resistance R_{es} and sheath capacitance Cs in parallel) and the base impedance Z_b (comprising $R_b > R_{es}$ and C_b; S. D. Bale et al. 2008, 2016). Similarly, the base impedance Z_b comprises a base resistance and a base capacitance, also connected in parallel. These two impedances are further connected in parallel, resulting in an equivalent impedance that can be expressed as

$$Z = \frac{R_{es}}{1 + 2\pi i f R_{es} C}, \tag{3}$$

where R_{es} represents the effective sheath resistance (sheath resistance R_s and antenna resistance R_p $\frac{R_p}{R_s} \approx 0.01 \sim 0.2$) and C represents the equivalent capacitance of the circuit. This electrical model is consistent with the circuit description used in Figure 1 of S. D. Bale et al. (2016), where the antenna is coupled to the plasma through both resistive and capacitive mechanisms and also interacts with the spacecraft electrically.

The main difference between Equations (3) and (2) lies in the introduction of the concept of effective resistance based on the expression in Equation (2), which is the core idea of this paper. If the effective resistance in Equation (3) is set to $R_{es} = \infty$, Equation (3) reduces to Equation (2); this limiting case does not match PSP observations. We propose a modified shot noise model in this paper to more accurately represent the physical processes involved. In the following sections, we will focus on discussing how this resistance varies with heliocentric distance.

In Figure 1, we use the traditional expression for impedance of the antenna in an isotropic plasma, as shown by the blue line, with its expression given by $Z = (i\omega C_{\rm ant})^{-1}$ (N. Meyer-Vernet & C. Perche 1989; M. Martinović et al. 2016; N. Meyer-Vernet et al. 2017; X. Zheng et al. 2024a, 2024b). In this figure, we present a comprehensive comparison and fitting analysis of the noise power spectral density (V^2) across a range of frequencies. This analysis is crucial for validating the accuracy and adaptability of our noise modeling framework under different parameter regimes.

In Figure 2, the left column (panels (a1), (a2), and (a3)) displays the total observed noise power spectral density, marked with black star symbols. These observed spectra are shown together with the modeled contributions from several distinct noise sources. These include electron thermal noise, charge impact noise, proton noise, instrument noise, and galactic background noise. Each of these components plays a different role in shaping the total noise profile, and their individual modeling is essential for isolating the dominant sources under various observational conditions. The right column of the figure, corresponding to panels (b1), (b2), and (b3), focuses specifically on the shot noise—primarily generated by the collisions of electrons and protons with the spacecraft. Here, we compare the observed impact noise with the results of a fitted analytical model. This model incorporates key electrical parameters of the antenna system, namely the effective sheath resistance R_{es},

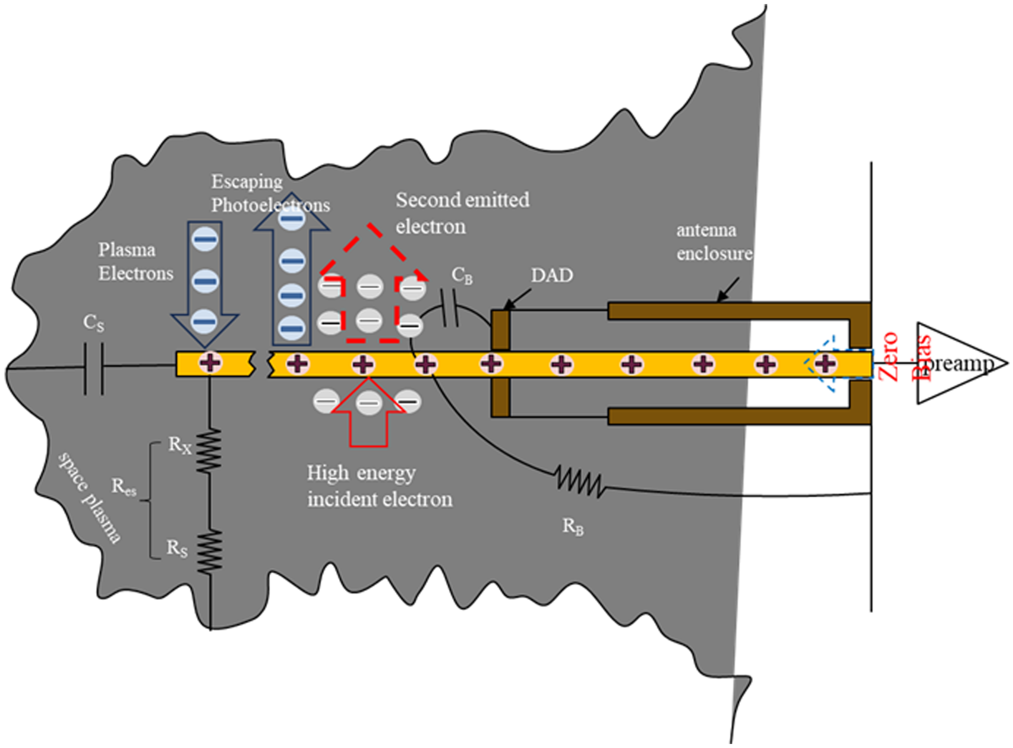

Figure 1. Schematic of the coupling model between a zero-bias antenna and the space plasma. This model is derived from theoretical calculations, incorporating key components such as sheath capacitance and effective sheath resistance. Additionally, it accounts for various elements including escaping electrons, plasma electrons, photoelectrons, and second electrons (W. Ember et al. 2024b).

sheath capacitance C_s, and frequency f. By adjusting these parameters, we can evaluate how well the model replicates the measured impact noise and assess the sensitivity of the results to variations in sheath properties.

In panel (b2), the asterisks represent the residual spectrum obtained by subtracting the modeled electron noise and proton noise from the total observational data. This subtraction isolates the impact noise component, allowing for a direct comparison with the theoretical model. In panel (b2), the pink line shows the fitted curve of the impact noise after accounting for the presence of antenna sheath resistance. This adjustment significantly affects the spectral shape, especially at lower frequencies, and is critical for accurately describing the observations at low frequencies. The same pink fitting curve appears again in panel (a2) to visually link the fitting result with the total noise decomposition shown in the left column.

The three example cases (a1/b1, a2/b2, and a3/b3) demonstrate how the inferred value of sheath capacitance changes depending on whether sheath resistance is included in the model fitting. In panel (a1) ($f > f_p$), the recalibrated capacitance remains consistent with the original estimate, indicating minimal impact of sheath resistance under those conditions. In panel (a2) ($f > f_p$), the recalibrated capacitance obtained after including R_{es} is smaller than the original value derived without accounting for sheath resistance. In contrast, panel (a3) shows a recalibrated capacitance that is larger than the original, suggesting that neglecting sheath resistance in such cases would significantly underestimate the system's reactive properties. Tests indicate that resistance and capacitance affect model fitting in a coupled manner: an increase in one estimate tends to reduce the inferred value of the other, with the deviation depending significantly on the chosen algorithm. In this study, the estimated capacitance was about 1.2% higher than the ideal antenna capacitance, causing the inferred resistance to be slightly lower than its ideal value.

3. Results and Discussion

3.1. The Radial Profile of Effective Impedance

We apply the calibrated shot noise model (as described in Section 2) to calculate the sheath resistance and capacitance using data from PSP Encounters 4 through 8. We use these encounters as the FIELDS instrument was operating under unbiased conditions for these times. Figure 3 presents the resulting resistance and capacitance derived from the calibrated shot noise analysis. Panels (a) through (f) respectively display the following: (a) the sheath resistance fitted using shot noise, (b) the electron current, (c) the photoelectron energy obtained by multiplying the sheath resistance and electron current, (d) the Debye length, (e) the antenna capacitance calculated from plasma parameters, and (f) the capacitance derived from the shot noise fitting.

To investigate how these parameters vary with radial distance from the Sun, the results are binned in intervals of 5 solar radial ($5\,r_s$), and the mean and standard deviation are calculated for each bin. $V_{\rm ph} = R_s{}^*I_e$, where $V_{\rm ph}$ is the photoelectron energy and $I_e = A\langle v\rangle en/4$ is the thermal electron current on the antenna. Here, A is the antenna surface area, n is the electron density, e is the elementary charge, and $\langle v\rangle$ is the average thermal speed of electrons.

As shown in Figure 3(a), the sheath resistance R_{es} increases (in conversation with J.W. Bonnell) with radial distance from the Sun and follows a trend of $R_{es} \propto r^{2.59\pm0.11}$. Figure 3(b) presents the variation of the thermal electron current I_e with radial distance, with a fitted relationship of $I_e \propto r^{-2.569\,\pm\,0.15}$. This result is consistent with theoretical expectations, since

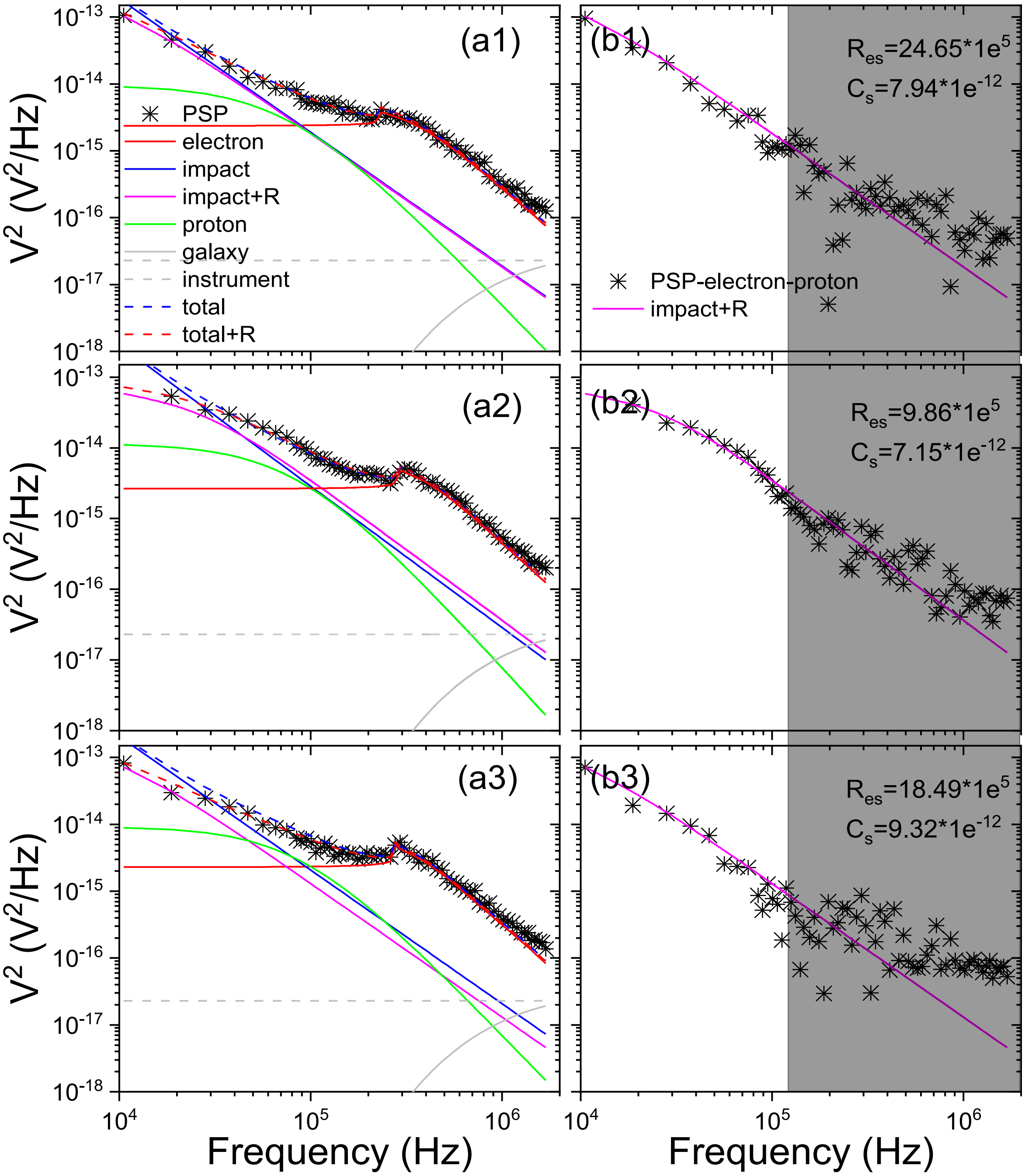

Figure 2. QTN fits to LFR observations. Panels (a1)–(a3) represent the total noise model, and panels (b1)–(b3) represent the shot noise. The figure shows the results after separating electron noise, proton noise, instrument noise, and galactic noise. The right panels show examples of shot noise fitting. The pink line in the figure represents the fitting result, while the star-shaped points indicate the shot noise observations after other noises have been removed; the shaded area shows when shot noise falls below 10% of the total signal.

$I_e \propto n_e * \langle v \rangle$, where the electron density $n_e \propto r^{-2}$ (Y. Whang & C. C. Chang 1965), and the electron thermal velocity $v_{\rm th} = \sqrt{\frac{2k_{\rm B}T_e}{m_e}}$ scales as $\propto r^{-0.59}$ in slow solar wind (Š. Štverák et al. 2015). Moreover, statistical studies show that PSP Encounters 2–13 indicate an overall scaling of $v_{\rm th} \propto r^{-0.67}$ under typical solar wind conditions (M. Maksimovic et al. 2020; M. Liu et al. 2023; X. Zheng et al. 2024a, 2024b). Additionally, panel 2(c) shows the calculated photoelectron energy $V_{\rm ph} = R_{es} * I_e$, with a fitted scaling of $V_{\rm ph} \propto r^{-0.18 \pm 0.01}$. However, this value is slightly higher than recent studies, which may be mainly due to the limited observational data used in this work. In addition, as shown in Figure 1, secondary electrons may play a significant role near the Sun, which deserves further attention in subsequent analyses (M. F. Diaz-Aguado et al. 2019, 2020, 2021b).

Figure 3(d) presents the variation of the Debye length ($\lambda_D = \sqrt{\frac{\epsilon_0 k_{\rm B} T_e}{n_e e^2}}$) with radial distance from the Sun. The results show that the Debye length increases with distance, exhibiting a power-law relationship of $\lambda_D \propto r^{0.42 \pm 0.02}$. The reason is that as the distance from the Sun increases, the electron density drops faster than the total electron temperature. Figures 3(e) and 2(f), respectively, display the antenna capacitance

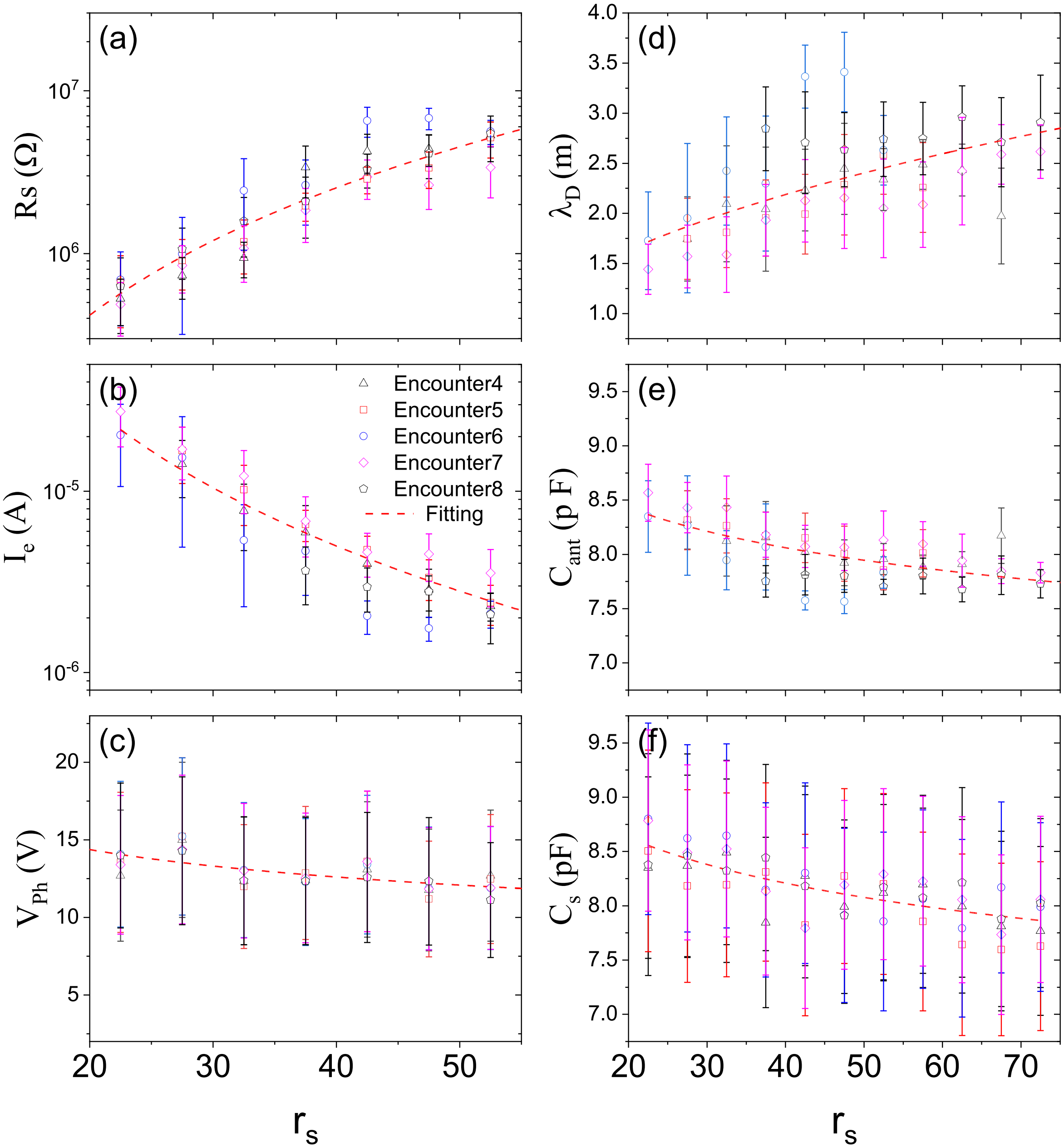

Figure 3. Radial variations of plasma and antenna parameters: (a) sheath capacitance and resistance, (b) electron current, (c) photoelectron energy, (d) Debye length, (e) antenna capacitance C_{ant} from plasma parameters, and (f) sheath capacitance C_s from inversion results.

calculated using the classical model $C_{\text{ant}} = \frac{\pi\epsilon_0 L_{\text{ant}}}{\log(\lambda_D / a_{\text{ant}})}$, where ε_0 is the permittivity of free space, L_{ant} is the antenna length and a_{ant} is the antenna radius, and the capacitance C is inferred from the calibrated shot noise model based on Equation (3). The fitted results show that both capacitance estimates vary with solar distance as $\propto \mathrm{r}^{-0.064 \pm 0.005}$ and $\propto r^{-0.072 \pm 0.001}$, respectively. The close agreement between the two methods indicates that the shot noise model provides a reliable estimate of the antenna capacitance. If the capacitance C obtained from Equation (3) is interpreted as the sheath capacitance C_s, then the results suggest that $C_{\text{ant}} \approx C_s$.

3.2. The Impact of Shot Noise

We use the shot noise model to fit and derive the effective sheath resistance R_{es} and sheath capacitance C_s in Figure 3. In this section, we will explore in detail the key factors that influence the inversion results of plasma shot noise, as well as the impact of sheath resistance and capacitance on the shot noise power spectrum. The influence of R_{es} and C_s on the shot noise power spectrum and the coupling model between the zero-biased antenna and the space plasma is illustrated in Figure 4.

Figures 4(a) and 3(b), respectively, show the effects of sheath resistance and sheath capacitance on the power spectral density of shot noise. The plasma parameters used in the calculations are set to an electron density of $n_e = 500\ \text{cm}^{-3}$ and an electron temperature of $T_e = 20$ eV. In Figure 4(a), the sheath capacitance is fixed at $C_s = 7.94{\cdot}10^{-12}$ F, while the sheath resistance is gradually increased from $4.66{\cdot}10^5$ Ω to infinity. The results show that for frequencies lower than $f/f_p \approx 0.5$, the power spectrum remains unchanged, while for frequencies above this value, the power spectrum increases as

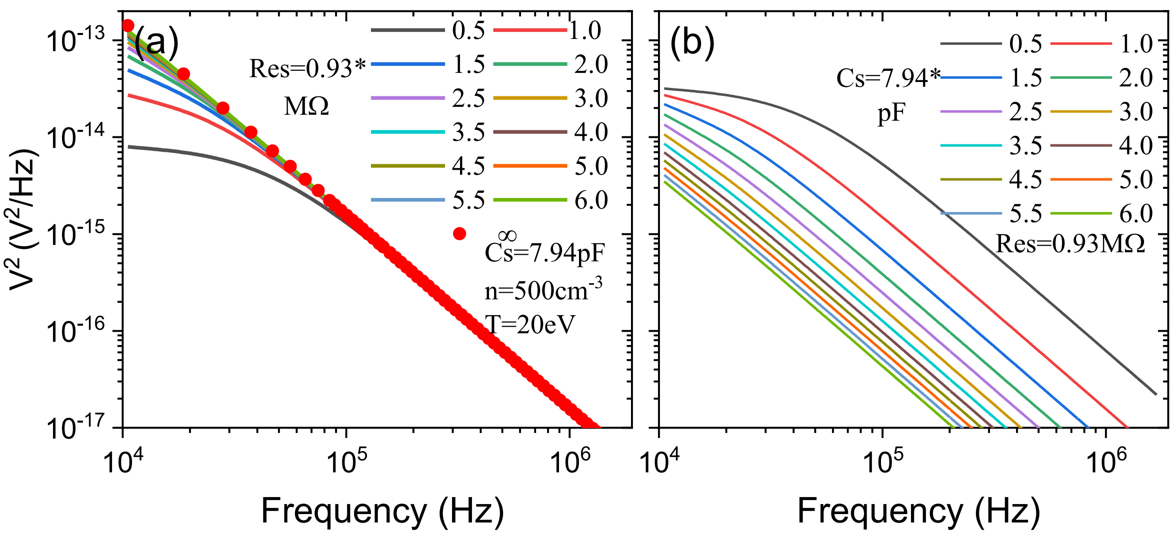

Figure 4. Effects of sheath parameters on shot noise: (a) sheath resistance R_{es}, with sheath capacitance C_s held fixed and (b) sheath capacitance C_s, with R_{es} held fixed. Each panel shows the resulting variations in shot noise spectra when only the indicated parameter is varied. And in panel (a), the normalized R_{es} is 0.93 MΩ; in panel (b), the normalized C_s is 7.94 pF.

resistance increases. Notably, when $R_{es} > 3.73 \cdot 10^6\ \Omega$ (i.e., $4 \times 9.32 \cdot 10^5\ \Omega$), the output of the shot noise reaches a stable state and no longer changes significantly. This explains why in Figure 4(a), the power spectrum stops increasing once the resistance exceeds approximately 4 MΩ—the system has reached a steady-state output for the given frequency range. The red dots in the figure correspond to the result for $R_{es} = \infty$, representing the assumption of the previous model (N. Meyer-Vernet 1983; M. Martinović et al. 2016). In Figure 4(b), the sheath resistance is fixed at $R_{es} = 9.32 \cdot 10^5\ \Omega$, while only the sheath capacitance C_s is varied to examine its influence on the shot noise power spectral density. The results indicate that as the sheath capacitance increases, the power spectral density of shot noise decreases significantly, demonstrating that increased capacitance suppresses the signal strength.

The results indicate that previous studies often neglected the influence of the equivalent sheath resistance, considering only the sheath capacitance. This assumption, however, is inconsistent with actual plasma measurements. Our findings show that under low-frequency conditions, the sheath resistance R_{es} critically affects the overall power spectrum, and this conclusion holds even for very hot or cold electrons (as tested at the 20 eV position in this paper).

4. Conclusions

In this work, a shot noise model incorporating the effect of sheath resistance is proposed based on observational results. The results show that this effect significantly impacts the fitting accuracy at low frequencies and in regions close to the Sun and thus cannot be neglected. The improved model not only enhances the agreement between QTN theory and observations but also provides a more accurate and reliable tool for QTN-based data inversion of PSP and other electric field antennas.

The results shown here are also intended to enable future studies, primarily by expanding this model to account for biased antenna signals (which require extra consideration of the biased current I_{biase}). We determined the radial profile of the capacitance C_S ($C_s \propto r^{-0.072 \pm 0.001}$) in the inner heliosphere and the radial resistance R_s profile ($R_S \propto r^{2.59 \pm 0.02}$). Furthermore, we analyzed how the electron current and photoelectron potential vary with radial distance from the Sun. The results indicate that the electron current decreases with distance following a power-law relationship of ($I_e \propto r^{-2.56 \pm 0.15}$), while the photoelectron potential shows a slower decline, scaling as $V_{\mathrm{ph}} \propto r^{-0.189 \pm 0.01}$.

Finally, we discussed the impact of the effective sheath resistance R_{es} and sheath capacitance C_s on power spectral density at low frequency ($f/f_p < 0.5$). The results show that when R_{es} increases, the power spectroscopy tends to increase in this frequency range, and when R_{es} exceeds 4 MΩ ($n = 500$, $Te = 20$ eV), the power spectrum remains nearly unchanged. Additionally, the study also indicates that when C_s increases, the power spectroscopy tends to decrease. These results verify the extended model for QTN spectroscopy on the PSP mission, which is of significant importance for future studies on the inversion of space plasma parameters.

Acknowledgments

This work was supported by the National Natural Science Foundation of China (42188101, 42441808, 42405133, 42474204), the Guangdong Pearl River Talent Program (2019QN01G838), and Shenzhen Science and Technology Program (grant JCYJ20210324104810027), the National Natural Science Foundation of China Distinguished Overseas Young Talents Program, the Frontier Scientific Research Program of Deep Space Exploration Laboratory (2022-QYKYJH-GCXD-004). V.P. acknowledges the project 21GRD02 BIOSPHERE from the European Partnership on Metrology, co-financed by the European Union's Horizon Europe Research and Innovation Programmer and by the participating states. M.M.M. and K.G.K. were financially supported by NASA grants: 80NSSC22K1011, 80NSSC19K1390, 80NSSC23K0693, 80NSSC19K0829, and 80NSSC24K0724. We would like to acknowledge Dr. Stuart Bale, Dr. Marc Pulupa, and Dr. J. W. Bonnell (UC Berkeley) for providing the FIELDS/QTNFIELDS/QTN data. Additionally, we thank the Parker Solar Probe mission team for making the SPAN data available for this study.

Data Availability Statement

PSP FIELDS LFR data are available at https://research.ssl.berkeley.edu/data/psp/data/sci/fields/l2/rfs_lfr/, and the M. Moncuquet et al. (2020) data are available at https://research.ssl.berkeley.edu/data/psp/data/sci/fields/l3/sqtn_rfs_V1V2/. The solar wind data can be availed at http://sweap.cfa.harvard.edu/pub/data/sci/sweap/spi/L3. For the QTN spectroscopy, we have just used the V1_V2 data.

Appendix A
Data Sample Sets

To facilitate the statistical analysis of the results, we performed a large-sample data analysis. Specifically, we utilized both data acquired without current bias and data acquired with current bias, as well as different fitting methods, as summarized in Table A1. It should be noted that in the table, "Z25" refers to the calibration shot noise method used in this study; "M20" refers to the method from reference M. Moncuquet et al. (2020); and "Z24" refers to the method provided in reference X. Zheng et al. (2024a). Additionally, for the "QTN" row in the first column of the table, we applied a 1 minute median averaging to the unbiased data from E4 to E8, while this processing was not applied to the other data.

Table A1
Sample Sizes of All Data and the Inversion Methods Used

Period	Sample	Biased/Unbiased	Fitting Method
QTN (E4∼E8)	≈670	Unbiased	Z25
Encounter 4	172,000	…	M20
Encounter 5	160,000	…	M20
Encounter 6	185,000	…	M20
Encounter 7	267,000	…	M20
Encounter 8	960	Unbiased	Z24

Appendix B
The Photoelectron Current and Voltage

For the receiving antenna, the total current can be written as (D. P. Cauffman & D. A. Gurnett 1972; N. Meyer-Vernet et al. 2017; M. F. Diaz-Aguado et al. 2021a)

$$I_{\text{total}} = I_{\text{ph}} + I_e + I_{se} + I_{\text{ion}} + I_{\text{bias}} + \ldots = 0.$$

For the photoelectron sheath ($V_{\text{flot}} > 0$), the sheath resistance is given by

$$R_s = \frac{V_{\text{ph}}}{|I_{\text{ph}}|} = \frac{V_{\text{ph}}}{|\, I_e + I_{se} - I_i - I_{\text{Bias}} \,|}.$$

The electron and ion currents are

$$I_e = eSn_e\sqrt{\frac{k_B T_e}{2\pi m_e}}\exp\left(\frac{e\phi}{k_B T_e}\right)$$

$$I_i = eSn_i\sqrt{\frac{k_B T_i}{2\pi m_i}}\left[2\sqrt{\frac{-e\phi}{k_B T_i}} + \exp\left(\frac{-e\phi}{k_B T_i}\right)\text{erf}\,c\left(\frac{-e\phi}{k_B T_i}\right)\right].$$

Since $I_e \gg I_i$ and the data we use is unbiased $I_{\text{biase}} = 0$, we also have $I_e \gg I_{se}$. Therefore, $|I_{\text{ph}}| = |\, I_e \,| \Rightarrow V_{\text{ph}} = R_{es} \,|\, I_e \,|$

ORCID iDs

Xianming Zheng https://orcid.org/0009-0005-7089-9749
Mihailo M. Martinović https://orcid.org/0000-0002-7365-0472
Kristopher G. Klein https://orcid.org/0000-0001-6038-1923
Viviane Pierrard https://orcid.org/0000-0001-5014-7682
Yutian Chi https://orcid.org/0000-0001-9315-4487
Bingkun Yu https://orcid.org/0000-0003-2758-1960
Xianghui Xue https://orcid.org/0000-0002-4541-9900

References

Bale, S. D., Goetz, K., Harvey, P. R., et al. 2016, SSRv, 204, 49
Bale, S. D., Ullrich, R., Goetz, K., et al. 2008, SSRv, 136, 529
Case, A. W., Kasper, J. C., Stevens, M. L., et al. 2020, ApJS, 246, 43
Cauffman, D. P., & Gurnett, D. A. 1972, SSRv, 13, 369
Dazzi, P., Issautier, K., Meyer-Vernet, N., Henri, P., & Martinović, M. 2025, JGRA, 130, e2024JA033325
Diaz-Aguado, M. F., Bonnell, J. W., Bale, S. D., Wang, J., & Gruntman, M. 2021a, JGRA, 126, e28688
Diaz-Aguado, M. F., Bonnell, J. W., Bale, S. D., Wang, J., & Gruntman, M. 2021b, JGRA, 126, e28689
Diaz-Aguado, M. F., Bonnell, J. W., Bale, S. D., et al. 2019, JSpRo, 56, 248
Diaz-Aguado, M. F., Bonnell, J. W., Bale, S. D., et al. 2020, JSpRo, 57, 793
Ember, W., Pulupa, M., & Bale, S. D. 2024b, in 2024 United States National Committee of URSI National Radio Science Meeting (USNC-URSI NRSM), Quantifying the Effects of Electron Shot Noise on a Current Biased Antenna (IEEE), 163
Ember, W., Pulupa, M., Martinović, M., et al. 2024a, Authorea Preprints
Fox, N., Velli, M. C., Bale, S. D., et al. 2016, SSRv, 204, 7
Gurnett, D. 1998, GMS, 103, 121
Issautier, K., Meyer-Vernet, N., Moncuquet, M., & Hoang, S. 1996, GeoRL, 23, 1649
Issautier, K., Meyer-Vernet, N., Moncuquet, M., Hoang, S., & McComas, D. 1999, JGRA, 104, 6691
Issautier, K., Perche, C., Hoang, S., et al. 2005, AdSpR, 35, 2141
Kasper, J. C., et al. 2016, SSRv, 204, 131
Kellogg, P. J. 1981, PlPh, 23, 735
Laframboise, J., & Parker, L. 1973, PhFl, 16, 629
Le Chat, G., Issautier, K., Meyer-Vernet, N., & Hoang, S. 2011, SoPh, 271, 141
Lin, R. P., Anderson, K. A., Ashford, S., et al. 1995, SSRv, 71, 125
Liu, M., Issautier, K., Meyer-Vernet, N., et al. 2021, A&A, 650, A14
Liu, M., Issautier, K., Moncuquet, M., et al. 2023, A&A, 674, A49
Livi, R., Larson, D. E., Kasper, J. C., et al. 2022, ApJ, 938, 138
Maksimovic, M., Bale, S. D., Berčič, L., et al. 2020, ApJS, 246, 62
Martinović, M. 2016, PhD thesis, Univ. Belgrade
Martinović, M., Zaslavsky, A., Maksimović, M., et al. 2016, JGRA, 121, 129
Martinović, M. M., Klein, K. G., Gramze, S. R., et al. 2020, JGRA, 125, e28113
Martinović, M. M., Dordević, A. R., Klein, K. G., et al. 2022, JGRA, 127, e30182
McComas, D., Alexander, N., Angold, N., et al. 2016, SSRv, 204, 187
Meyer-Vernet, N. 1983, JGRA, 88, 8081
Meyer-Vernet, N., Issautier, K., & Moncuquet, M. 2017, JGRA, 122, 7925
Meyer-Vernet, N., & Lecacheux, A. 2024, RNAAS, 8, 92
Meyer-Vernet, N., & Perche, C. 1989, JGRA, 94, 2405
Moncuquet, M., Lecacheux, A., Meyer-Vernet, N., Cecconi, B., & Kurth, W. S. 2005, GeoRL, 32, L20S02
Moncuquet, M., Meyer-Vernet, N., & Hoang, S. 1995, JGRA, 100, 21697
Moncuquet, M., Meyer-Vernet, N., Issautier, K., et al. 2020, ApJS, 246, 44
Pulupa, M., Bale, S., Salem, C., & Horaites, K. 2014, JGRA, 119, 647
Pulupa, M., Bale, S. D., Bonnell, J. W., et al. 2017, JGRA, 122, 2836
Sauvaud, J. A., Larson, D., Aoustin, C., et al. 2008, SSRv, 136, 227
Štverák, Š., Trávníček, P. M., & Hellinger, P. 2015, JGRA, 120, 8177
Vourlidas, A., Howard, R. A., Plunkett, S. P., et al. 2016, SSRv, 204, 83
Whang, Y., & Chang, C. C. 1965, JGR, 70, 4175
Whittlesey, P. L., Larson, D. E., Kasper, J. C., et al. 2020, ApJS, 246, 74
Young, D., et al. 2005, in The Cassini-Huygens Mission: Orbiter In Situ Investigations Volume, ed. C. T. Russell, Vol. 2 (Springer Science & Business Media), 104
Zheng, X., Liu, K., Martinović, M., et al. 2024a, ApJ, 963, 154
Zheng, X., Martinović, M. M., Pierrard, V., et al. 2024b, ApJ, 977, 39
Zheng, X., Martinović, M. M., Klein, K. G., et al. 2025, ApJ, 985, 114
Zouganelis, I., Maksimovic, M., Meyer-Vernet, N., et al. 2010, RaSc, 45, RS1005